JOURNAL OF PROPULSION AND POWER
Vol. 15, No. 3, May–June 1999

Computation of Vortex Shedding in Solid Rocket Motors Using Time-Dependent Turbulence Model

A. Kourta*
IMFT, F-31400 Toulouse, France
and
CERFACS, F-31057 Toulouse, France

This paper is devoted to the computation of turbulent effects on the aeroacoustic interaction in solid rocket motors. The purpose is to establish a simulation method that estimates the vortex-shedding and acoustic-wave interaction. To perform these unsteady computations, turbulent motion is taken into account by a first-order model based on a nonlinear relationship between time-dependent Reynolds stresses and velocity gradients. Model coefficients are explicit functions of both strain and rotation. This model is applied to the computation of two simplified configurations of a rocket booster. To better evaluate the turbulent effects, computations are presented with and without a turbulence model. In both configurations, the natural unsteadiness of the flow is captured and the comparisons with numerical and experimental data are presented. The interaction between vortex shedding and acoustics is described and the turbulence effects are characterized.

I. Introduction

SHEAR layers that develop behind sharp solid discontinuities produce instabilities and vortex-shedding that are able to interfere with acoustic waves in a confined chamber. This phenomenon is addressed in the present paper. Such a situation can be found in large solid-propellant rocket motors, such as space boosters. Indeed, the periodic vortex shedding in rocket motors[1–4] is the result of a strong coupling between the instability of mean shear flow and acoustic modes in the chamber. The feedback from the acoustic waves provides the control signal for the aerodynamic instability. This phenomenon was investigated by solving the unsteady compressible Navier–Stokes equations without introducing turbulence models.[5–12] Interesting results have been found for the aeroacoustic coupling, but in view of full-scale computations, turbulence must be addressed if one wants realistic predictions of the instability frequencies and of the resulting levels of pressure and thrust oscillations.

For practical configurations, such as full-scale solid rocket motors, direct numerical simulation and large-eddy simulation can hardly be used mainly because of the expensive cost required by a suitable resolution, particularly in connection with boundary conditions. Therefore, the use of Reynolds-averaged Navier–Stokes equations, containing turbulence models, is currently the only viable way to predict the mean and turbulent quantities in complex flows. Sabnis et al.[13,14] used ensemble-averaged Navier–Stokes equations to predict the steady mean flow in solid-propellant rocket motor chambers by using an implicit solver and the two-equation Jones–Launder k-ε turbulence model. With this turbulence model, the turbulence level is twice overpredicted. Calculations performed by Beddini,[15] using a parabolic form of the viscous equations of motion together with a Reynolds stress turbulence model, also predicted a similar discrepancy. Dunlap et al.[16] suggested that the overprediction for the injection-driven flow may reflect turbulent length-scale differences not accounted for in the turbulence models used. Their measurements reveal that values in the porous tube flow are less than half those in the pipe flow. This indicates that these models are not well adapted to these kinds of flows, and a more suitable model is needed, particularly when the flow presents injection wall and coherent structures. The simultaneous existence of the organized and disorganized structures in the flow is obvious. Thus, it seems necessary to make a distinction between the role played by each type of structure. The computations presented here are based on splitting the instantaneous motion into an unsteady ensemble-average motion and an incoherent random motion.[17,18] The first part is calculated and the second part is modeled.

The use of ensemble averaging leads to a set of equations looking identical to the one obtained with time averaging, so-called Reynolds averaging, except that the Reynolds shear stress is replaced by the ensemble-averaged shear stress, which can be interpreted as organized Reynolds stresses. In turbulence modeling, unknown turbulent correlations can be related algebraically to the mean flowfield (first-order models) or determined by their own dynamical transport equations (second-order models). The second-order models are attractive because they can simulate the transport of the individual correlations, and hence, contain physics missing in first-order models (anisotropy, etc.). Nevertheless, it is difficult to consistently model all of the higher-order turbulent correlations appearing in these second-moment dynamical equations. For practical calculations, first-order models are more convenient. However, the standard first-order models, such as the k-ε, which is the most popular one used in practical flow calculations, present two limits. The first limit is that the model coefficients are constant and are determined under equilibrium or isotropic turbulence conditions, thus, they are not universal. The second limit is that these models use Boussinesq's isotropic eddy–viscosity concept, which assumes that the unknown correlations are proportional to the mean velocity gradients. This concept fails for flows where the normal stresses play an important role. This suggests the need for a more general model for complex flows overcoming both limitations listed earlier. For these reasons, in steady-state and anisotropic flows, more general closure relations have been derived.[19–25] They contain both linear and nonlinear terms of the average velocity gradient. The same approach is extended to develop unsteady calculation. The presence of a nonlinear term allows better evaluation of the turbulent stress anisotropy, which can be important for unsteady flows. Moreover, the model coefficients are functions of flow characterstics and, hence, are time dependent.

This approach is used to compute the flow and the aeroacoustic interactions in two simplified configurations of the booster. The interaction between the aerodynamic instability and the acoustic mode is analyzed and the impact of the tubulence on this mechanism is characterized. In addition to this nonstationary modeling, an experimental study[26–28] and large eddy simulation (LES) method[29–32] are investigated for the same configurations. Results obtained in this study will be compared, when possible, with other studies.

Received Feb. 10, 1997; revision received Oct. 14, 1997; accepted for publication Sept. 8, 1998.

*Research Scientist, Av. du Prof. Camille Soula; also 42, avenue G. Coriolis.

II. Governing Equations

A. Decomposition

The starting point of the present approach is the decomposition of any instantaneous physical variable into coherent organized and incoherent random parts. Equations for the coherent part are obtained by performing an ensemble average of the instantaneous flow equations. The effects of the random part are introduced by using a suitable unsteady turbulence model. The following relation for the variables can be written:

$$\chi(x_k,t) = \hat{\chi}(x_k,t) + \chi_r(x_k,t) \tag{1}$$

where χ represents the instantaneous quantity, $\hat{\chi}$ represents the organized unsteadiness part that can be computed, and χ_r designates the random and incoherent fluctuations. This decomposition can be obtained by phase averaging, which is averaging over a large ensemble of points having the same phase. In particular, this decomposition is fully satisfied if pseudoperiodic components exist in the flow. Experimentally, it has been derived in many cases for single-frequency phenomena. It is more difficult to determine the situation for multifrequency phenomena, although, in this case, a special filtering operation, such as the one used by Brereton and Kodal,[33] can be performed. Theoretically, there is no restriction in deriving the suitable mathematical model, apart from the prescription of adequate boundary and initial conditions for each phase-averaged variable of the flow.

A condition to formally obtain adequate equations for the coherent motion is to impose a zero cross correlation

$$\widehat{(\hat{\chi}\cdot\chi_r)} = 0$$

between coherent and incoherent motions. This implies that only quadratic interactions will appear for the random part of the fluctuations, and that so-called Leonard stresses do not exist in these equations, not like in the conventional LES approach. Again, the special filtering procedure used by Brereton and Kodal[33] is applicable in an experimental study to measure such fluctuations in real flows. Under these assumptions, the resulting phase-averaged Navier–Stokes equations look identical to the Reynolds-averaged Navier–Stokes equations, except that the Reynolds shear stress is replaced by the phase-averaged shear stress.

In this study no filtering is used to establish the equations. The coherent part derived by the decomposition is general. In fact, for the numerical study, the efficiency of the decomposition is related to the turbulent model used. Such a decomposition between a coherent and incoherent part provides a set of partial differential equations that holds for all possible decompositions, satisfying the previously mentioned conditions. The specific problem corresponding to a given practical filtering is then defined through adequate boundary conditions and modeling for unknown correlations.

In the present work, the generally admitted mass-weighted averaging procedure is retained for all transportable variables in compressible flows:

$$\tilde{\chi} = \widehat{\rho\chi}/\hat{\rho} \tag{2}$$

where $\tilde{\chi}$, the mass-weighted phase average, is time dependent.

B. Coherent Flow Equations

Phase-averaged Navier–Stokes equations for a two-dimensional or axisymmetric nonswirling flow can be written as a vector equation. Hence, motion equations are written as

$$\frac{\partial W}{\partial t} + \frac{\partial F}{\partial x_1} + \frac{1}{x_2^n}\frac{\partial\left(x_2^n G\right)}{\partial x_2} = H \tag{3}$$

$$W = \begin{bmatrix} \hat{\rho} \\ \hat{\rho}\tilde{U}_1 \\ \hat{\rho}\tilde{U}_2 \\ \hat{\rho}\tilde{E} \end{bmatrix}, \qquad F = \begin{bmatrix} \hat{\rho}\tilde{U}_1 \\ \hat{\rho}\tilde{U}_1\tilde{U}_1 + \sigma_{11} \\ \hat{\rho}\tilde{U}_1\tilde{U}_2 + \sigma_{12} \\ (\hat{\rho}\tilde{E} + \sigma_{11})\tilde{U}_1 + \sigma_{12}\tilde{U}_2 - \lambda\dfrac{\partial\tilde{T}}{\partial x_1} \end{bmatrix}$$

$$G = \begin{bmatrix} \hat{\rho}\tilde{U}_2 \\ \hat{\rho}\tilde{U}_1\tilde{U}_2 + \sigma_{21} \\ \hat{\rho}\tilde{U}_2\tilde{U}_2 + \sigma_{22} \\ (\hat{\rho}\tilde{E} + \sigma_{22})\tilde{U}_2 + \sigma_{12}\tilde{U}_1 - \lambda\dfrac{\partial\tilde{T}}{\partial x_2} \end{bmatrix}$$

$$H = \frac{n}{x_2}\left\{\begin{matrix} 0 \\ 0 \\ \hat{P} - \mu\left[2\dfrac{\tilde{U}_2}{x_2} - \dfrac{2}{3}\left(\dfrac{\partial\tilde{U}_1}{\partial x_1} + \dfrac{1}{x_2}\dfrac{\partial x_2\tilde{U}_2}{\partial x_2}\right)\right] \\ 0 \end{matrix}\right\}$$

with

$$n = \begin{cases} 1 & \text{axi} \\ 0 & \text{two dimensional} \end{cases}$$

The shear stress tensor is given by

$$\sigma_{ij} = \left[\hat{P} + \frac{2}{3}\mu\left(\frac{\partial\tilde{U}_1}{\partial x_1} + \frac{1}{x_2^n}\frac{\partial x_2^n\tilde{U}_2}{\partial x_2}\right)\right]\delta_{ij} - 2\mu S_{ij} + \hat{\rho}\widetilde{u_iu_j} \tag{4}$$

C. Turbulence model

The use of ensemble averaging leads to an open set of equations. The time-dependent approach gives identical equations with the same number of unknown correlations to be modeled as for the classical stationary approach. Consequently, modeling of the time-dependent correlations, $\widetilde{u_iu_j}$ [Eq. (4)], can be achieved in the same way as for the classical time-mean correlations. Therefore, both the eddy-viscosity concept and second-order modeling can be considered. For reasons that were listed in Sec. I, an appropriate first-order model is used in the present study.

The closure law of turbulent stresses that was used is similar to the one obtained by Zhu and Shih,[22] or Shih et al.,[23] and it was used by these authors to compute steady flows. Assuming that the new correlations depend on the phase-averaged velocity gradients, turbulent length, and velocity scales, a closure relationship is derived by using the invariance theory. Using the realizability conditions,[34] the coefficients are found to be functions of the time-scale ratio of the turbulent to the phase-averaged strain rate and of the time scale of the turbulent to the phase-averaged rotation rate.

The turbulent length and velocity scales are characterized by the phase-averaged turbulent kinetic energy $\tilde{k}$ and dissipation $\tilde{\varepsilon}$, hence, the phase-averaged correlations $\widetilde{u_iu_j}$ are expressed as:

$$\widetilde{u_iu_j} = \Phi_{ij}\left(\frac{\partial\tilde{U}_i}{\partial x_j}, \tilde{k}, \tilde{\varepsilon}\right) \tag{5}$$

Using the same derivation as used by Zhu and Shih[22] (see also Shih et al.[23]), the closure model can be obtained as follows[35]:

$$\hat{\rho}\widetilde{u_iu_j} = -2\cdot\mu_t S_{ij} + T_{ij} + \frac{2}{3}\left[\hat{\rho}\tilde{k} + \mu_t\left(\frac{\partial\tilde{U}_1}{\partial x_1} + \frac{1}{x_2^n}\frac{\partial x_2^n\tilde{U}_2}{\partial x_2}\right)\right]\delta_{ij} \tag{6}$$

with

$$\mu_t = C_\mu(\hat{\rho}\tilde{k}^2/\tilde{\varepsilon})$$

and by taking only a quadratic form of T_{ij}, we finally obtain:

$$T_{ij} = \frac{\hat{\rho}\tilde{k}^3}{\tilde{\varepsilon}^2} f(\eta, \xi)\left[C_{\upsilon 1}\left(\frac{\partial \tilde{U}_i}{\partial x_k}\frac{\partial \tilde{U}_k}{\partial x_j} + \frac{\partial \tilde{U}_j}{\partial x_k}\frac{\partial \tilde{U}_k}{\partial x_i} - \frac{2}{3}\Pi\delta_{ij}\right)\right.$$
$$\left. + C_{\upsilon 2}\left(\frac{\partial \tilde{U}_i}{\partial x_k}\frac{\partial \tilde{U}_j}{\partial x_k} - \frac{1}{3}\Pi'\delta_{ij}\right) + C_{\upsilon 3}\left(\frac{\partial \tilde{U}_k}{\partial x_i}\frac{\partial \tilde{U}_k}{\partial x_j} - \frac{1}{3}\Pi'\delta_{ij}\right)\right] \tag{7}$$

f and C_μ are dependent on the time-scale ratio of the turbulence to the phase-averaged strain rate η, and on the time-scale ratio of the turbulence to the phase-averaged rotation ξ:

$$f(\eta, \xi) = 1\big/\left(A_2 + \eta^3 + \gamma_2\xi^3\right) \tag{8}$$

$$C_\mu(\eta, \xi) = \tfrac{2}{3}\big/(A_1 + \eta + \gamma_1\xi) \tag{9}$$

with

$$\Pi = \frac{\partial \tilde{U}_k}{\partial x_l}\frac{\partial \tilde{U}_l}{\partial x_k}, \qquad \Pi' = \frac{\partial \tilde{U}_k}{\partial x_l}\frac{\partial \tilde{U}_k}{\partial x_l}, \qquad \eta = \frac{\tilde{k}S}{\tilde{\varepsilon}}, \qquad \xi = \frac{\tilde{k}\Omega}{\tilde{\varepsilon}}$$

$$S = (2S_{ij}S_{ij})^{\frac{1}{2}}, \qquad S_{ij} = \frac{1}{2}\left(\frac{\partial \tilde{U}_i}{\partial x_j} + \frac{\partial \tilde{U}_j}{\partial x_i}\right)$$

$$\Omega = (2\Omega_{ij}\Omega_{ij})^{\frac{1}{2}}, \qquad \Omega_{ij} = \frac{1}{2}\left(\frac{\partial \tilde{U}_i}{\partial x_j} - \frac{\partial \tilde{U}_j}{\partial x_i}\right)$$

It is worthwhile to note that both C_μ and f depend on η and ξ. Generally, in previous work using the same kind of model, the time-scale ratio of the turbulence to the rotation ξ is not introduced in the coefficients C_μ and f. In this approach, the unsteady motion of the coherent structures involves the rotation effect on all coefficients, thus, all terms in Eqs. (8) and (9) are maintained in the computation and the model is, in fact, more complete than the ones usually retained for stationary mean flow computations.

To achieve the closure process, the phase-averaged turbulent kinetic energy of the turbulent motion and its phase-averaged dissipation ($\tilde{k}$, $\tilde{\varepsilon}$) must be determined by using two transport equations:

$$\frac{\partial W'}{\partial t} + \frac{\partial F'}{\partial x_1} + \frac{1}{x_2^n}\frac{\partial\left(x_2^n G'\right)}{\partial x_2} = H' \tag{10}$$

$$W' = \begin{bmatrix} \hat{\rho}\tilde{k} \\ \hat{\rho}\tilde{\varepsilon} \end{bmatrix}, \qquad F' = \begin{bmatrix} \hat{\rho}\tilde{k}\tilde{U}_1 - \left(\mu + \dfrac{\mu_t}{\sigma_k}\right)\dfrac{\partial \tilde{k}}{\partial x_1} \\ \hat{\rho}\tilde{\varepsilon}\tilde{U}_1 - \left(\mu + \dfrac{\mu_t}{\sigma_\varepsilon}\right)\dfrac{\partial \tilde{\varepsilon}}{\partial x_1} \end{bmatrix}$$

$$G' = \begin{bmatrix} \hat{\rho}\tilde{k}\tilde{U}_2 - \left(\mu + \dfrac{\mu_t}{\sigma_k}\right)\dfrac{\partial \tilde{k}}{\partial x_2} \\ \hat{\rho}\tilde{\varepsilon}\tilde{U}_2 - \left(\mu + \dfrac{\mu_t}{\sigma_\varepsilon}\right)\dfrac{\partial \tilde{\varepsilon}}{\partial x_2} \end{bmatrix}$$

$$H' = \begin{bmatrix} -\hat{\rho}\widetilde{u_i u_j}\dfrac{\partial \tilde{U}_i}{\partial x_j} - \hat{\rho}\tilde{\varepsilon} - D_1 \\ -C_{\varepsilon 1}\dfrac{\tilde{\varepsilon}}{\tilde{k}}\hat{\rho}\widetilde{u_i u_j}\dfrac{\partial \tilde{U}_i}{\partial x_j} - C_{\varepsilon 2} f_2 \dfrac{\hat{\rho}\tilde{\varepsilon}^2}{\tilde{k}} + D_2 \end{bmatrix}$$

To account for near-wall flow, the low-turbulent Reynolds number model having the same form as the Jones–Launder near-wall model[36] is used. The damping functions (f_μ of μ_t and f_2), and the new constants (D_1 and D_2), dependent on phase-averaging variables, are introduced:

$$f_\mu = \exp\left(\frac{-2.5}{1 + (R_t/50)}\right), \qquad f_2 = 1 - 0.3\exp\left[-(R_t)^2\right]$$
$$D_1 = 2\mu\left(\frac{\partial\sqrt{\tilde{k}}}{\partial x_2}\right)^2, \qquad D_2 = -2\mu\mu_t\left(\frac{\partial^2 \tilde{U}}{\partial x_2^2}\right)^2 \tag{11}$$

where

$$R_t = \hat{\rho}\tilde{k}^2/\mu\tilde{\varepsilon}$$

The low-turbulent Reynolds number model is only applied on the solid wall and not on the propellant surface. This is consistent with analytical results derived by Chaouat[37] for an injecting surface. The model coefficients are given next: $C_{\varepsilon_1} = 1.44$, $C_{\varepsilon_2} = 1.92$, $\sigma_k = 1.0$, $\sigma_\varepsilon = 1.3$, $C_{\upsilon 1} = -4$, $C_{\upsilon 2} = 13$, $C_{\upsilon 3} = -2$, $A_1 = 1.25$, $A_2 = 1000$, $\gamma_1 = 0.9$, and $\gamma_2 = 1$.

It can be noted that if we only conserve the linear part of the model ($C_{\upsilon 1}$, $C_{\upsilon 2}$, and $C_{\upsilon 3}$ equal to zero), and C_μ equal to 0.09, we obtain the standard Jones–Launder model.

The most outstanding difference with a model used to compute the steady-state developed by Shih et al.[23] is the use of low Reynolds number modeling in contrast with the use of wall function.

The use of this approach for the unsteady flows with organized structures is motivated by the fact that this model is more general than classical first-order models and is not limited to Boussinesq's isotropic eddy-viscosity concept. This feature makes it more adequate for predicting the unsteadiness.

III. Methodology

A. Numerical method

The numerical method used is a version of the explicit MacCormack scheme.[9] It consists of a predictor–corrector approach. For each time step, forward or backward approximations for the inviscid part are used, and central differences are used for the viscous terms. The two steps of the scheme can be written as follows:

For the predictor step:

$$\Delta W^{(m)} = -\Delta t\left[\frac{\partial F^{(m)}}{\partial x_1} + \frac{1}{x_2^n}\frac{\partial x_2^n G^{(m)}}{\partial x_2} - H^{(m)}\right]$$
$$W^{\overline{(m+1)}} = W^{(m)} + \Delta W^{\overline{(m+1)}} \tag{12}$$

For the corrector step:

$$\Delta W^{(m+1)} = -\Delta t\left[\frac{\partial F^{\overline{(m+1)}}}{\partial x_1} + \frac{1}{x_2^n}\frac{\partial x_2^n G^{\overline{(m+1)}}}{\partial x_2} - H^{\overline{(m+1)}}\right]$$
$$W^{(m+1)} = \frac{1}{2}\left[W^{(m)} + W^{\overline{(m+1)}} + \Delta W^{(m+1)}\right] \tag{13}$$

The scheme is time and space second-order accurate. In the present numerical code, it is also possible to use the implicit method based on a Gauss–Seidel line relaxation technique or the flux-splitting technique, but to compute an unsteady flow, it has been shown that computation without these options is more accurate and practical because both of these techniques induce damping effects.[9]

B. Computational Domains

Two laboratory-scale motors are of concern here. The first is a two-dimensional planar solid rocket motor called C1, and the second is axisymmetric and named C1x.

The computational configuration of the C1 rocket booster is presented in Fig. 1. The grid (318 × 31) is the same as that used by Lupoglazoff and Vuillot.[12] The length of the chamber was chosen in such a way that the first mode frequency was close to the critical frequency of the shear layer ($f_{cr} = 1320$ Hz).[9,12] The length of this plane motor is 0.47 m with 0.2-m-length grain. The same configuration in a three dimensional case with the same mesh in (x_1, x_2) directions was used for computations with an LES approach by Silvestrini et al.[29] and Silvestrini.[30]

The axisymmetric test case geometry (C1x) is close to the C1 configuration. However, it has a higher length (0.785 m) with 0.35-m-length grain. It corresponds to a whistling motor that was investigated for numerous firing tests at ONERA.[26–28] This motor has been designed to produce sustained vortex shedding-driven oscillations to validate the numerical codes. The firing time considered here corresponds to a 3-mm propergol burned layer. The geometry and grid are presented in Fig. 1. The grid size is (597 × 49). This test case (grid and specifications) was supplied by ONERA.

C. Boundary and Initial Conditions

The boundary conditions imposed to rocket boosters are given in Table 1.

The no-slip condition is imposed at the inert wall, where the velocity and normal pressure gradient are equal to zero. At the injecting wall, the mass flow rate, temperature, and zero tangential velocity are specified. For the outflow boundary, the supersonic classical first-order extrapolations are used. Concerning turbulent quantities, $\tilde{k}$ and $\tilde{\varepsilon}$ are set to zero at the wall.

Table 1 Boundary conditions

Head end	Aft end	Internal side	External side
No slip	Supersonic outflow	Symmetry	A1: injecting wall
—	—	—	A2: no slip condition

Note: A1 and A2 are given in Fig. 1.

For initial conditions, computations are started from rest for the case without a turbulence model. The solutions obtained in these steps are used as initial conditions to perform computations with the turbulence model.

D. Physical Values

Table 2 presents the physical values used for both cases. In this table, ρ_p is the propellant density, V_c is the propellant burning rate, $\dot{m}$ is the injection mass flow rate $(\rho v)_{\text{inj}}$, T_f is the flame temperature, a is the speed of sound, R is the perfect gas constant, μ is the molecular viscosity, γ is the ratio of specific heats, and Pr is the Prandtl number.

For the C1 planar motor, the time step used is equal to $dt = 1.623 \times 10^{-7}$ s; 350,000 iterations were performed. The computation was done on a Convex C220 computer, and for one time step, 1.1 CPU seconds were needed. For the axisymmetric case (C1x), the time step was $dt = 1 \times 10^{-7}$ s; 500,000 iterations were performed.

IV. Computational Results

A. Unsteady Navier–Stokes Computations Without Turbulence Model

The code was first tested with unsteady Navier–Stokes solutions to assess its validity and isolate the specific effect of the turbulence modeling.

The velocity and pressure signals obtained at different positions in the flow, for the C1 case, show the unsteady organized character of the flow. Figure 2 presents examples of pressure and velocity time histories. The corresponding spectra are also reported. These

Table 2 Physical values[a]

Case	ρ_p	V_c	$\dot{m}$	T_f	a	R	μ	γ	Pr
C1	1633	13×10^{-3}	21.201	3387	1075.43	299.53	36×10^{-5}	1.14	1
C1x	1586	4.18×10^{-3}	6.62948	2224	1031	384.513	7×10^{-5}	1.243	0.495

[a] S.I. units.

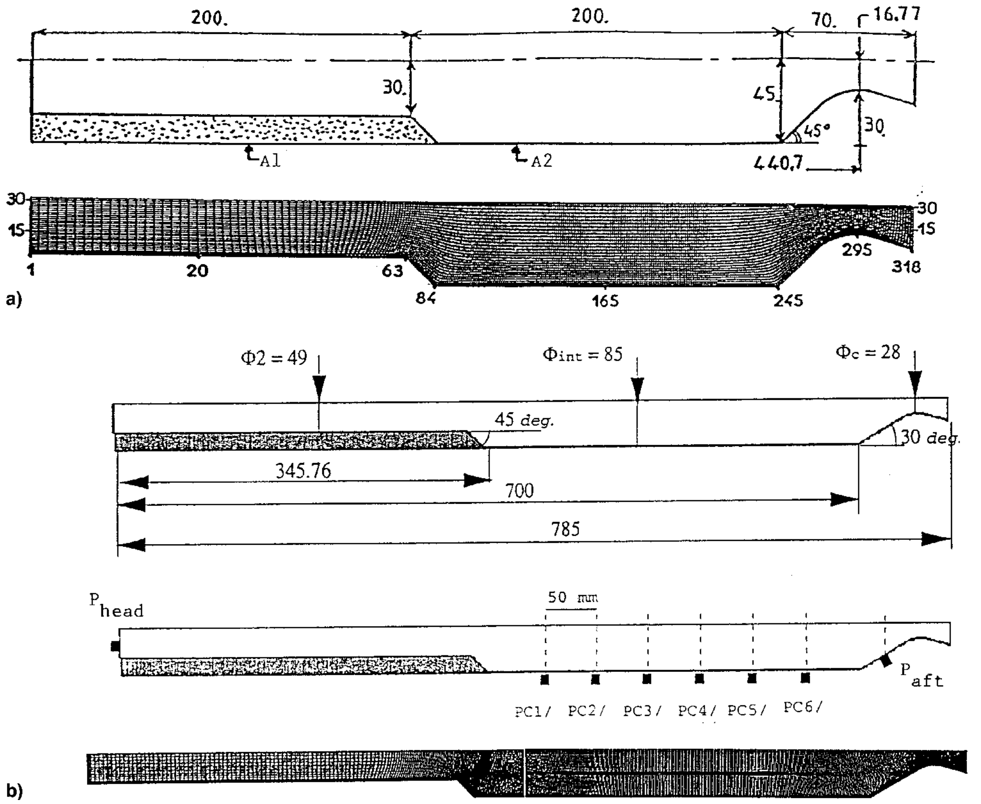

Fig. 1 Computational domains: a) C1 and b) C1x.

spectra show a monochromatic character of the signal with a high peak close to the second axial-mode frequency (2570 Hz). Vuillot et al.[38] and Silvestrini et al.[29] obtained the same periodic mechanism at approximately the same frequency. A comparison with their results has been made with good agreement. The coupling process is very sensitive to the position of the shear-layer origin (X_0). Lupoglazoff and Vuillot,[12] using Flandro's method, show that for 241 mm $\leq X_0 \leq$ 285 mm, mode $2L$ should be unstable, whereas mode $1L$ should be stable. The numerical simulation results are in agreement with their analytical evaluations, as X_0 is in this range.

Figure 3 presents the isovorticity contours during one period. In the mixing layer, coupled with acoustic oscillations, periodic vortex shedding occurs. This process is self-sustaining and well described by many previous authors (see, for example, Vuillot[4] or Kourta[9]).

In these first computations, comparisons are done with other numerical simulations and with analytical theories. For the C1x test case, we have the possibility to compare with experimental data. Pressure signals were measured at eight positions, including the head and end positions (Fig. 1 and Table 3). Pressure signals were recorded at the same positions. The problem is assumed to be axisymmetric.

Time histories of the pressure are plotted in Fig. 4. The signals are regular, but not monochromatic. They present the same shape and behaviors that are similar to those obtained experimentally by Refs. 26–28, and numerically by Refs. 30 and 38. Tables 4 and 5 present, respectively, the mean values and amplitude (zero-peak) of pressures. The amplitude is approximated using the rms value as defined by Kourta.[11] In these tables, the results are compared with numerical Navier–Stokes computations performed on the same mesh[30,38] and also with experimental data.[26,27] The mean values are in good agreement with experimental data. The head-end mean pressure is well predicted. Computations done by Silvestrini[30] slightly underestimate these values. It can be noticed that the mean pressure increases between the sixth sensor ($PC6$) and the aft end (P_{aft}). This indicates the existence of separation bubble upstream of the nozzle. Concerning the zero-peak ampliude levels (Table 5), these computations are in good agreement with the other ones for the same mesh. However, all of these numerical simulations overestimate the

Table 3 Pressure sensor positions

	P_{head}	$PC1$	$PC2$	$PC3$	$PC4$	$PC5$	$PC6$	P_{aft}
x, mm	0	400	450	500	550	600	650	720.5
y, mm	22	42.5	42.5	42.5	42.5	42.5	42.5	30.7

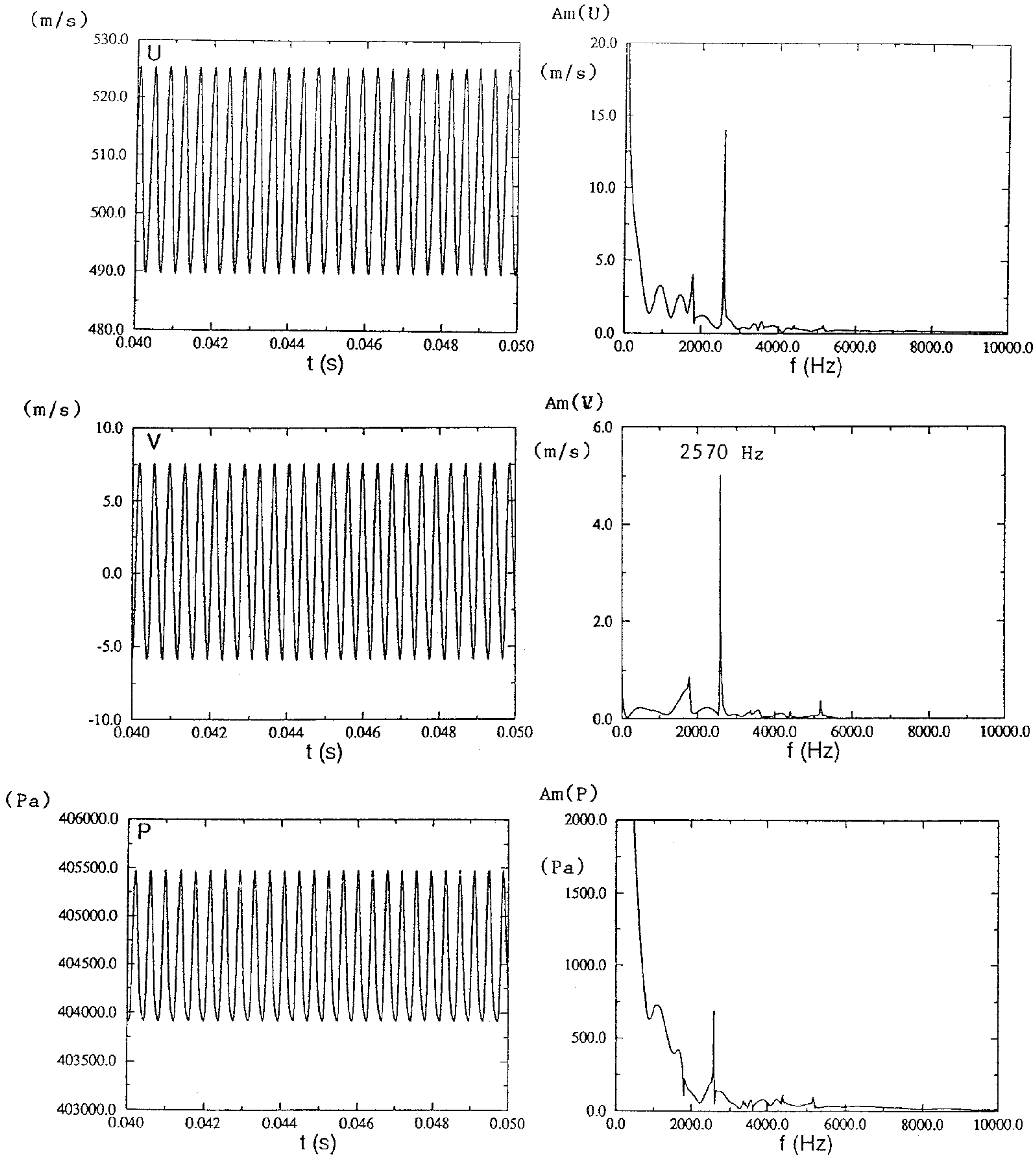

Fig. 2 Time histories and spectra of velocity and pressure (C1, without turbulence). $x_1/L = 0.78, x_2/L = 0.0824$.

Table 4 Mean values of pressure[a]

	P_{head}	$PC1$	$PC2$	$PC3$	$PC4$	$PC5$	$PC6$	P_{aft}
This study	9.525	9.233	9.233	9.233	9.231	9.230	9.231	9.241
Silvestrini[30]	9.436	9.141	9.140	9.139	9.139	9.138	9.136	9.158
Experiment[26,27]	9.52	9.22	—	—	—	—	9.22	9.23

[a] Bar.

Table 5 Zero-peak amplitude of pressure[a]

	P_{head}	$PC1$	$PC2$	$PC3$	$PC4$	$PC5$	$PC6$	P_{aft}
This study	0.028	0.018	0.014	0.015	0.025	0.028	0.051	0.047
Silvestrini[30]	0.039	0.026	0.021	0.026	0.032	0.033	0.057	0.048
Vuillot et al.[38]	0.027	0.022	0.019	0.017	0.024	0.042	0.037	0.029
Experiment[26,27]	0.008	0.005	0.007	0.010	0.007	0.013	0.013	0.018

[a] Bar.

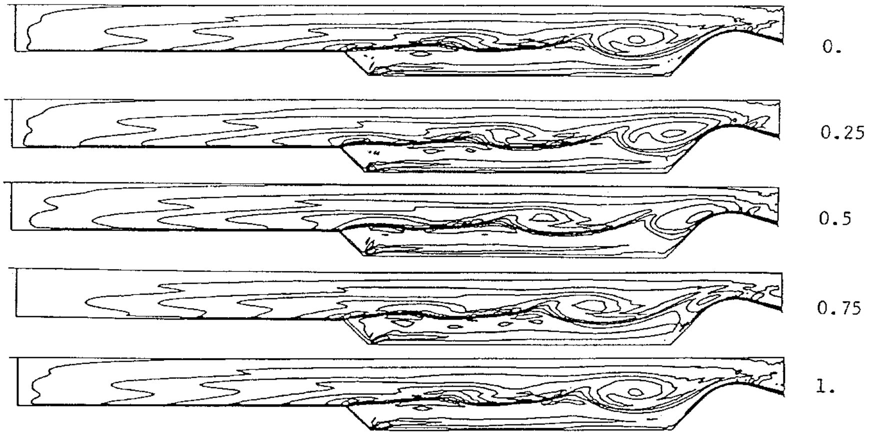

Fig. 3 Isovorticity during one period (second longitudinal mode) (C1, without turbulence).

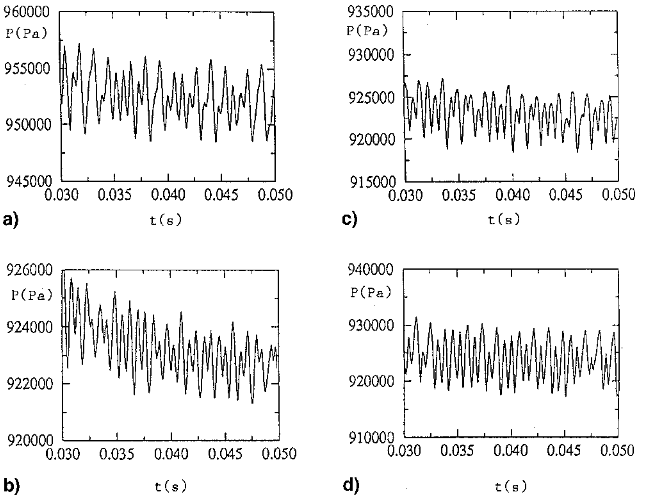

Fig. 4 Time histories of the pressure (C1x, without turbulence): a) P_{head}, b) $PC2$, c) $PC5$, and d) P_{aft}.

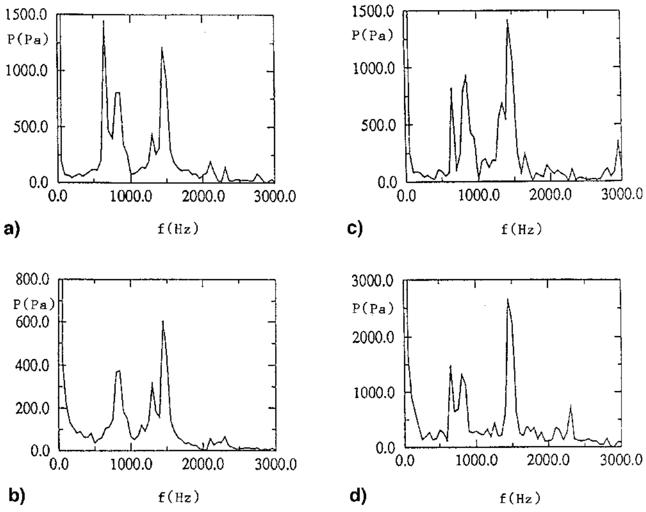

Fig. 5 Spectra of the pressure (C1x, without turbulence): a) P_{head}, b) $PC2$, c) $PC5$, and d) P_{aft}.

experimental levels. This overestimation can be a result of two physical phenomena not considered in the numerical simulations: turbulence or three-dimensional effects.

The spectra, corresponding to the pressure signals, obtained with fast Fourier transform, are plotted in Fig. 5. These spectra exhibit many peaks. The longitudinal acoustic modes, up to the fourth, are present. The higher peak corresponds to the second axial mode (1300 Hz). Another important peak is also detected and corresponds to 800 Hz. This frequency is not related to the acoustics in the booster. The same frequencies are also detected by numerical simulations of Vuillot et al.[38] and of Silvestrini et al.[29] The 800-Hz frequency starts to be important near and after the second pressure sensor. It is related to the oscillations induced by the curvature effect near the nozzle and imposed to the recirculation in the corner.

Figure 6 shows the isovorticity contours during one period corresponding to a second axial mode (1300 Hz). They show that the flow corresponds to a confined mixing layer characterized by periodic vortex shedding as a consequence of Kelvin–Helmholtz instability. During the period, two vortices are generated and only one vortex is absorbed by the nozzle. This indicates that the vortex shedding

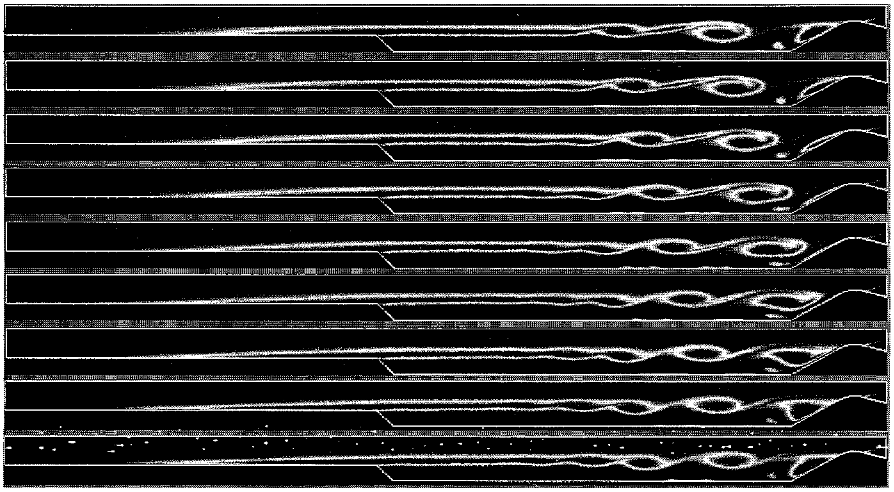

Fig. 6 Isovorticity during one period (second axial mode) (C1x, without turbulence).

frequency corresponds to a fourth axial mode (2600 Hz) and that the pairing mechanism exists. The resulting vortices are related to the second axial mode. The same vortex mechanisms are also observed by Silvestrini[30] and Vuillot et al.[38] In this figure it is also observed that there is near-wall instability owing to the curvature and characterized by unsteady zone in the corner of the nozzle.

These numerical results, and also those obtained by Silvestrini[30] and Vuillot et al.,[38] show that the vortex shedding is coupled with the fourth acoustic mode, whereas the experiment[26,28] show no coupling. As pointed out by Vuillot and Lupoglazoff,[31] the chosen time into the firing (3-mm burned) corresponds to the first regime, comprised between ignition and approximately 1 s into the firing. This regime appears to be weakly coupled with the chamber acoustics. It is believed that nonintense vortex shedding is taking place at this time point, contrary to the second regime that starts after the 9–10-mm-burned point. Vuillot and Lupoglazoff believed that this behavior resulted from large turbulence levels in the early part of the firing. In this case, the discordance between the computations and the experiment can be related to the absence of turbulence in the computed equations.

B. Unsteady Navier–Stokes Computations with Turbulence Model

The modeling of turbulent effects is an important key in the ability of a numerical simulation to accurately predict the aeroacoustic interaction in the solid rocket motors. It is needed to predict both the instabilities frequencies and amplitude levels. For this reason, the time-dependent turbulence model is used to study both motor configurations previously computed without a turbulent model. Special attention is given to evaluate the turbulence effects on this interaction.

For the C1 configuration, the time evolution of the thrust and corresponding spectrum are presented on Fig. 7. The signal is not regular compared with the viscous nonturbulent case where the time evolutions were monochromatic. Turbulence produces a superimposition of another organized motion to the vortex-shedding one. The difference in the nonturbulent case is the appearance of another frequency (1910 Hz). The peak at the frequency close to the second longitudinal mode is also detected in the present turbulent case.

Figure 8 presents the spectra of the longitudinal velocity component at four points located downstream of the shear-layer origin. Two points are near the solid wall (Figs. 8a and 8b) and the two others are in the shear layer. The spectra show peaks at 1910 and 2600 Hz, both in the near-wall region and in the shear layer. In the near-wall region, the peak at 1910 Hz is more intense than that in the shear layer, and can be higher than the other frequency peaks (Fig. 8b). In the shear-layer region, the second longitudinal mode is the predominant frequency.

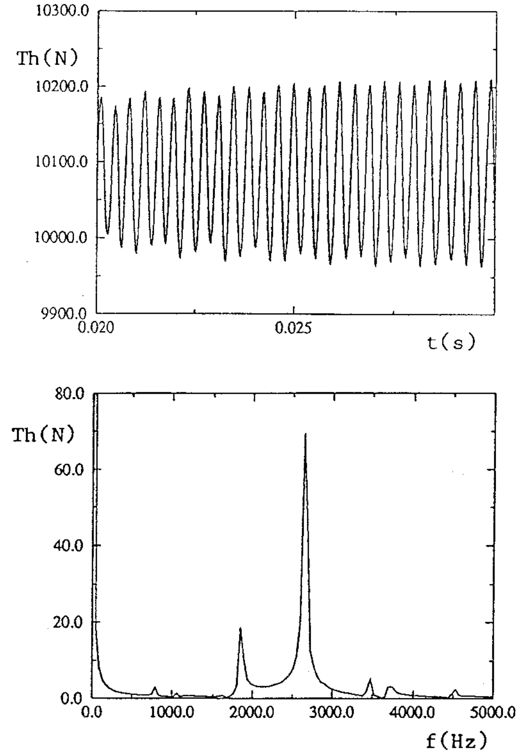

Fig. 7 Time history and spectrum of the thrust (C1, with turbulence).

The time evolution of the isovorticity contours (not shown here) during one period corresponding to the second longitudinal acoustic mode confirms that this acoustic mode controls the flow and the vortex shedding. However, the structures are less marked than in the case without turbulence and the intensity of the concentrated vorticity is smaller. The observed values of the turbulent viscosity was on the order of 100 times that of the molecular viscosity in the shear layer. The coherent part of the turbulent kinetic energy is periodic, as with all other turbulent quantities. The global behavior of the chamber is controlled by the second longitudinal acoustic mode.

The other source of instability observed in the chamber is characterized by a frequency of 1910 Hz. This can be interpreted as a secondary instability that affects mainly the near-wall flow. It appears as a bulk oscillation in this region, which affects the whole chamber. The origin of this instability can be associated with the separation of the boundary layer upstream of the nozzle, as found by Silvestrini et al.[29] and Silvestrini[30] using the LES approach. It is produced by compression effects in the nozzle and most likely enhanced by the presence of the turbulence yielding a thicker boundary

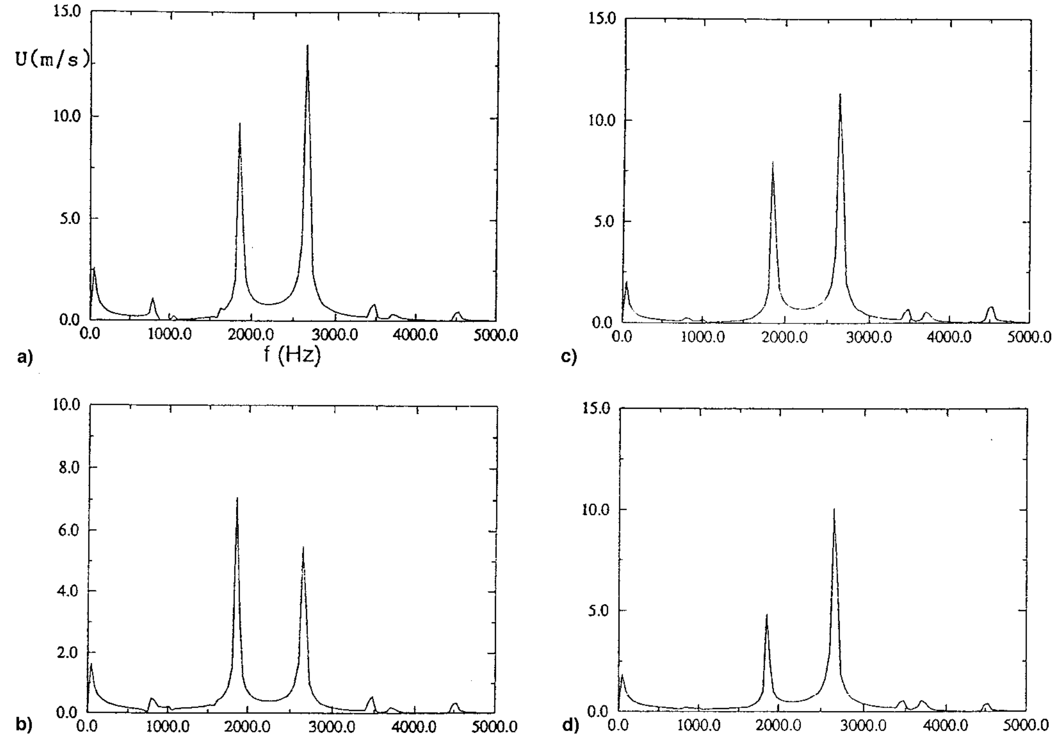

Fig. 8 Spectra of the U-velocity component (C1, with turbulence): a) $x_1/L = 0.79, x_2/L = 0.0076$; b) $x_1/L = 0.73, x_2/L = 0.0075$; c) $x_1/L = 0.78, x_2/L = 0.0824$; d) $x_1/L = 0.73, x_2/L = 0.0820$.

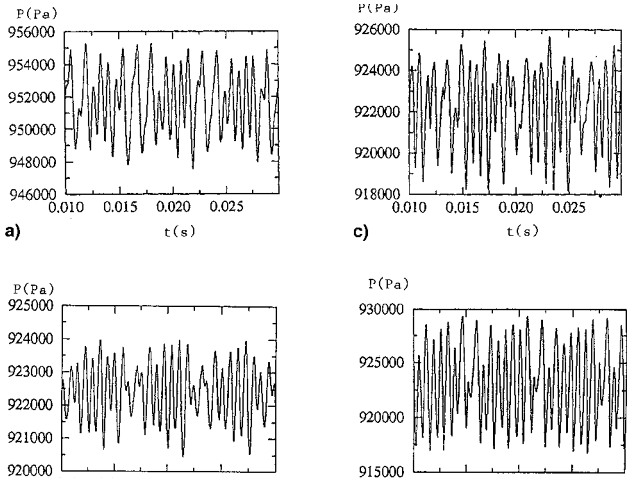

Fig. 9 Time histories of the pressure (C1x, with turbulence): a) P_{head}, b) $PC2$, c) $PC5$, and d) P_{aft}.

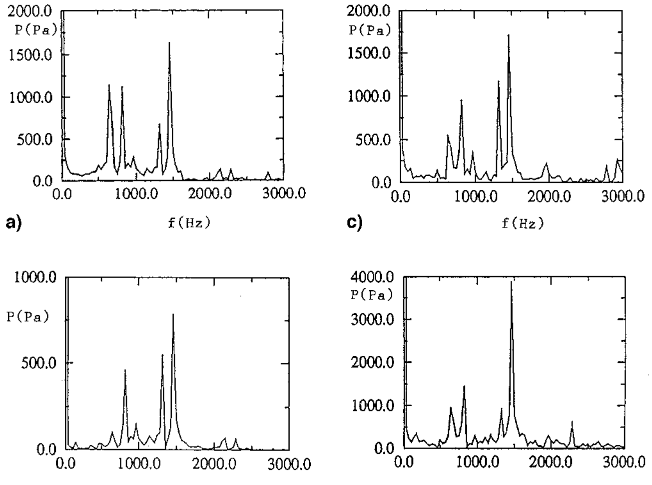

Fig. 10 Spectra of the pressure (C1x, with turbulence): a) P_{head}, b) $PC2$, c) $PC5$, and d) P_{aft}.

layer along the nozzle wall. For this reason, this instability was not detected in a previous simulation performed in the nonturbulent case.

Also, with the turbulence model, an attenuation of the oscillatory levels is observed. Silvestrini et al.,[29] with a three-dimensional LES simulation, did not detect such attenuation. In this study,[29] the high amplitude of the oscillation levels seemed to indicate that the turbulent viscosity is very small compared with the molecular one, and, in this case, the turbulence does not play any significant role in this flow. This last result contradicted the modification of frequency in this simulation. Lupoglazoff and Vuillot[32] performed a two-dimensional simulation by applying LES models derived for three-dimensional problems without extension to the two-dimensional case. They obtained even less attenuation than in the present work. In their paper, however, the attenuation is more important with the Smagorinsky model than with Lesieur's structure function model. A significant scatter exists between all of the values obtained for the turbulent viscosity, and moreover, near-wall treatment is not always properly set up. For all of these reasons, it is not possible to definitively conclude on this aspect, but the results obtained from the present model do not suffer from some of the same drawbacks as the previous ones. The quality of the frequency and amplitude response of the model argues for the validity of the results of this model.

The time-dependent turbulence model is then applied to the axisymmetric whistling motor, C1x. Time histories of the pressure are plotted in Fig. 9, and corresponding spectra in Fig. 10. There are no significant differences between these results and those obtained without turbulence. The signals have the same shape and behaviors. Tables 6 and 7 present, respectively, the mean values and amplitude (zero-peak) of pressures. In these tables, computations done with and without a turbulence model are compared with experimental data.[26–28] The predicted mean values of pressure are in good agreement with experimental data. The results obtained using a turbulence model seem more favorable. Without a turbulence model, the mean pressure increases between the sixth sensor ($PC6$) and the aft end (P_{aft}), showing the existence of a recirculation zone upstream of the nozzle. Concerning the zero-peak amplitude levels (Table 7), with and without a turbulence model, numerical simulations overestimate the experimental levels. This overestimation can be a result of the three-dimensional mean flow effects that were most likely important in this case, but were not included in our simulation. The fact that the results obtained with and without a turbulence model are approximately the same, indicate that the turbulence does not play an important role for the firing time selected in this simulation.

Figure 11 shows the isovorticity contours during one period corresponding to a second axial acoustic mode. The same remarks made for the case without a turbulent model are still valid in the present case. The vortex shedding is controlled by the fourth axial acoustic mode, and pairing is observed. Hence, as it was observed that without a turbulence model, acoustically coupled vortex shedding was taking place, which is not the case for the experiment.[26–28] The time evolution of the phase-averaged turbulent kinetic energy is plotted in Fig. 12. Its evolution follows the one observed for the phase-averaged mean flow. The higher-turbulence levels are observed between two vortices. The turbulence levels are small. The evolution of the turbulent viscosity is the same as the turbulent kinetic energy one. In the shear layer, the turbulent viscosity reaches its maximum level, and is between two and seven times that of the molecular viscosity value. This indicates that the presence of turbulence does not significantly enhance the effective diffusivity.

Table 6 Mean values of pressure[a]

	P_{head}	$PC1$	$PC2$	$PC3$	$PC4$	$PC5$	$PC6$	P_{aft}
Without turbulence	9.525	9.233	9.233	9.233	9.231	9.230	9.231	9.241
With turbulence	9.516	9.224	9.224	9.224	9.224	9.223	9.222	9.230
Experiment[26,27]	9.52	9.22	—	—	—	—	9.22	9.23

[a] Bar.

Table 7 Zero-peak altitude of pressure[a]

	P_{head}	$PC1$	$PC2$	$PC3$	$PC4$	$PC5$	$PC6$	P_{aft}
Without turbulence	0.028	0.018	0.014	0.015	0.025	0.028	0.051	0.047
With turbulence	0.026	0.017	0.011	0.013	0.024	0.025	0.025	0.048
Experiment[26,27]	0.008	0.005	0.007	0.010	0.007	0.013	0.013	0.018

[a] Bar.

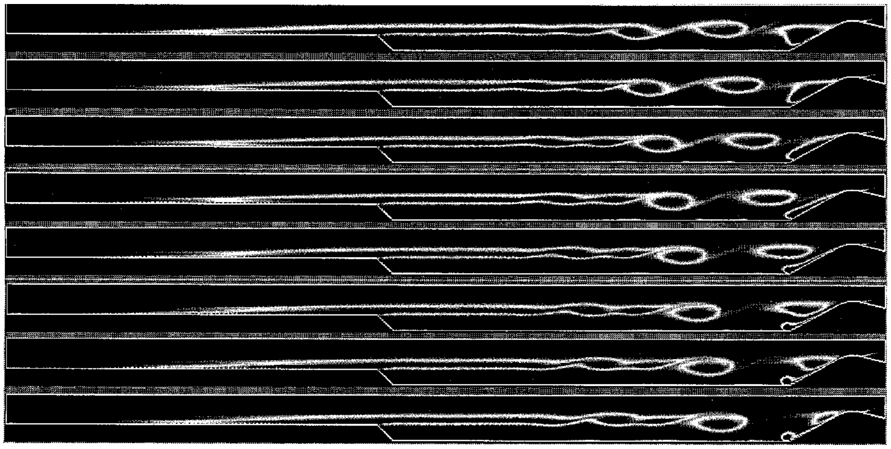

Fig. 11 Isovorticity during one period (second axial mode) (C1x, with turbulence).

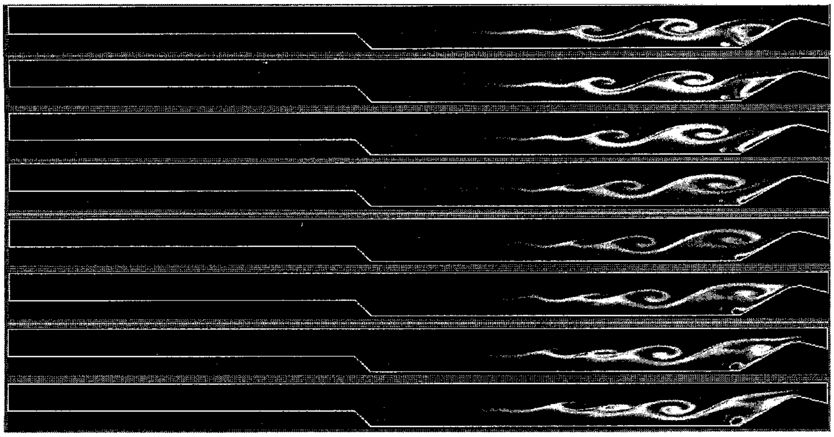

Fig. 12 Isoturbulent kinetic energy during one period (C1x, with turbulence).

Vuillot and Lupoglazoff[31] applied LES models, derived for a three-dimensional calculation (Smagorinsky and Lesieur models), to two-dimensional axisymmetric configurations (0- and 3-mm burned). They studied the 0-mm-burned (ignition) configuration and found that the computed flowfields showed a net decrease in oscillatory amplitude in agreement with experiments. For the 3-mm-burned configuration, they observed that the oscillatory amplitudes do not decrease, contrary to the experiments. This last numerical result is in agreement with the present work. However, Vuillot et al.[38] observed that in the experiments, the acoustic coupling is detected in four cases over 11. In these cases, the experimental spectra show the fourth acoustic mode, which can be the vortex shedding frequency. Such situations correspond to the acoustic coupling in the booster. If so, the agreement between the computation and the experiment is good, but the question of onset of this coupling is still unresolved.

V. Conclusions

The present study is devoted to the simulation of the vortex shedding in turbulent shear flows and its interaction with acoustic modes inside the solid-propellant rocket motors. To correctly predict these kind of flows, a time-dependent turbulent model is used. The unknown correlations are expressed in terms of higher-order relationships of the phase-averaged velocity gradients. An important behavior of the present model is that the coefficients are not constant but are functions of the flow mechanisms. They depend on the time-scale ratio η and ξ, and thus, are time dependent.

The numerical simulation is used to analyze the flow inside two simplified rocket motor configurations where vortex shedding has been observed. Computations are done with and without a turbulence model. In this last case, the time-dependent turbulence model is applied.

The first case computed, C1, is a two-dimensional configuration. The vortex shedding is correctly predicted with and without turbulence, and agreement with other numerical simulations and analytical results is obtained. In both situations, the vortex shedding is controlled by the second axial acoustic mode. The introduction of a turbulent model leads to important modifications. Compared to a nonturbulent viscous simulation, the monochromatic state does not exist in the turbulent case. Two frequencies are detected; one of them corresponds to a second longitudinal acoustic mode. Apparently, the flow and vortex shedding are controlled by the second longitudinal acoustic mode, as it was in the case of nonturbulent simulations. The second mode is more intense in the near-wall region and is associated with compression effects in the nozzle. In this configuration, the use of a turbulence model improves the prediction of the flow instabilities with correct frequencies and levels.

The second geometry corresponds to the ONERA experiment (C1x). The aeroacoustic interactions are predicted. The vortex shedding is captured. Its frequency corresponds to the fourth axial acoustic mode. The pairing mechanism characterized by the second axial acoustic mode frequency is also detected. In this case, the introduction of the turbulence model does not strongly modify the results. For the firing time chosen, the turbulence does not play an important role. The difference between our simulations and experiments in the amplitude levels can be because the axisymmetric assumption is done in the simulation and seems inadequate in this case.

This turbulence model presents one promising way to perform full-scale computations for unsteady flows. However, more improvements and validations are needed to capture more complex situations, such as the initiation of oscillations or the influence of three-dimensional phenomena.

Acknowledgments

In connection with the development of the Ariane 5 P230 solid rocket motor, this work is part of research program managed by ONERA and supported by CNES, CNES/ONERA Contract 93/3040. Part of the computations were done with the help of an IDRIS (CNRS) computer. Special thanks go to H. C. Boisson and H. Ha Minh for valuable comments.

References

[1] Flandro, G., and Jacobs, H., "Vortex Generated Sound in Cavities," AIAA Paper 73-1014, Oct. 1973.

[2] Flandro, G., "Vortex Driving Mechanism in Oscillatory Rocket Flows," *Journal of Propulsion and Power*, Vol. 3, No. 3, 1986, pp. 206–214.

[3] Brown, R., Dunlap, R., Young, S., and Waugh, R., "Vortex Shedding as a Source of Acoustic Energy in Segmented Solid Rocket," *Journal of Spacecraft*, Vol. 8, No. 4, 1981, pp. 312–319.

[4] Vuillot, F., "Vortex Shedding Phenomena in Solid Rocket Motors," *Journal of Propulsion and Power*, Vol. 11, No. 4, 1995, pp. 626–639.

[5] Jou, W., and Menon, S., "Simulations of Ramjet Combustor Flow Fields Part II—Origin of Pressure Oscillations," AIAA Paper 87-1422, June 1987.

[6] Menon, S., and Jou, W., "Numerical Simulation of Oscillatory Cold Flows in an Axisymmetric Ramjet Combustor," *Journal of Propulsion and Power*, Vol. 6, No. 5, 1990, pp. 525–534.

[7] Menon, S., and Jou, W., "Large-Eddy Simulations of Combustion Instability in an Axisymmetric Ramjet Combustor," AIAA Paper 90-0267, Jan. 1990.

[8] Kailasanath, K., Gardner, J., Boris, J., and Oran, E., "Acoustic Vortex Interactions and Low Frequency Oscillations in Axisymmetric Combustors," AIAA Paper 87-0165, Jan. 1987.

[9] Kourta, A., "Acoustic-Mean Flow Interaction and Vortex Shedding in Solid Rocket Motors," *International Journal for Numerical Methods in Fluids*, Vol. 22, 1996, pp. 449–465.

[10] Kourta, A., "Vortex Shedding in Solid Rocket Motors," AIAA Paper 95-0727, Jan. 1995.

[11] Kourta, A., "Vortex Shedding in Segmented Solid Rocket Motors," *Journal of Propulsion and Power*, Vol. 12, No. 2, 1996, pp. 371–376.

[12] Lupoglazoff, N., and Vuillot, F., "Numerical Simulation of Vortex Shedding Phenomenon in 2D Test Case Solid Rocket Motors," AIAA Paper 92-0776, Jan. 1992.

[13] Sabnis, J. S., Gibeling, H., and McDonald, H., "Navier-Stokes Analysis of Solid Propellant Rocket Motor Internal Flows," AIAA Paper 89-2558, July 1989.

[14] Sabnis, J. S., Madabhushi, R., Gibeling, H., and McDonald, H., "Vortex Shedding in Segmented Solid Rocket Motors," *Journal of Propulsion and Power*, Vol. 6, No. 6, 1989, pp. 657–664.

[15] Beddini, R. A., "Injection-Induced Flows in Porous-Walled Ducts," *AIAA Journal*, Vol. 24, No. 11, 1986, pp. 1766–1773.

[16] Dunlap, R., Blackner, A. M., Waugh, R. C., Brown, R. S., and Willoughby, P. G., "Internal Flow Field Studies in a Simulated Cylindrical Port Rocket Chamber," *Journal of Propulsion and Power*, Vol. 6, No. 6, 1990, pp. 690–704.

[17] Reynolds, W., and Hussain, A., "The Mechanics of an Organized Wave in Turbulent Shear Flow. Part 3. Theoretical Models and Comparisons with Experiments," *Journal of Fluid Mechanics*, Vol. 54, Pt. 2, 1972, pp. 263–288.

[18] HaMinh, H., and Kourta, A., "Semi-Deterministic Turbulence Modelling for Flows Dominated by Strong Organized Structures," *9th Symposium on Turbulent Shear Flows*, 1993, pp. 10-5(1–6).

[19] Pope, S., "A More General Effective-Viscosity Hypothesis," *Journal of Fluid Mechanics*, Vol. 72, Pt. 2, 1975, pp. 331–340.

[20] Speziale, C., "On Nonlinear K-l and K-ε Models of Turbulence," *Journal of Fluid Mechanics*, Vol. 178, 1987, pp. 459–475.

[21] Yoshizawa, A., "Statistical Analysis of the Deviation of the Reynolds Stress from Its Eddy-Viscosity Representation," *Physics of Fluids*, Vol. 27, No. 6, 1984, pp. 1377–1387.

[22] Zhu, J., and Shih, T., "Computation of Confined Coflow Jets with Three Turbulence Models," *International Journal for Numerical Methods in Fluids*, Vol. 19, 1994, pp. 939–956.

[23] Shih, T., Zhu, J., and Lumley, J., "A Realizable Reynolds Stress Algebraic Equation Model," NASA TM 105993, 1993.

[24] Taulbee, D., "An Improved Algebraic Reynolds Stress Model and Corresponding Nonlinear Stress Model," *Physics of Fluids A*, Vol. 4, No. 11, 1992, pp. 2555–2561.

[25] Yoshizawa, A., "Derivation of a Model Reynolds-Stress Transport Equation Using the Renormalization of the Eddy-Viscosity-Type Representation," *Physics of Fluids A*, Vol. 5, No. 3, 1993, pp. 707–715.

[26] Dupays, J., and Delfour, A., "Description du Montage LP2/C1-x et Résultats de la Campagne d'Essais 1994," ONERA, TR RT 61/6133 EY, 1995.

[27] Dupays, J., "Contribution à l'Etude du Rôle de la Phase Condensée dans la Stabilité d'un Propulseur à Propergol Solide pour Lanceur Spatial," Thèse de Doctorat de l'Institut National Polytechnique de Toulouse, Toulouse, France, 1996.

[28] Dupays, J., Prevost, M., Tarrin, P., and Vuillot, F., "Effects of Particulate Phase on Vortex Shedding Driven Oscillations in Solid Rocket Motors," AIAA Paper 96-3248, 1996.

[29] Silvestrini, J., Comte, P., and Lesieur, M., “Simulation de Grandes Echelles: Application aux Moteurs á Propergol Solide Segmentes,” *Conference on Propulsive Flows in Space Transportation Systems* (Bordeaux, France), 1995, pp. 205–220.

[30] Silvestrini, J., “Simulation de Grandes Echelles des Zones de Melange: Application á la Propulsion Solide des Lanceurs Spatiaux,” Thése de Doctorat de l’Institut National Polytechnique de Grenoble, Grenoble, France, 1996.

[31] Vuillot, F., and Lupoglazoff, N., “Combustion and Turbulent Flow Effects in 2D Unsteady Navier-Stokes Simulations of Oscillatory Solid Rocket Motors—First Applications,” AIAA Paper 96-0884, Jan. 1996.

[32] Lupoglazoff, N., and Vuillot, F., “Application de modéle de turbulence de Sous-Maille aux Cas Test C1 et C1x et Mise au Point d’un Module de Combustion Instationnaire” ONERA, TR RT 50/6133 EY, 1994.

[33] Brereton, G., and Kodal, A., “An Adaptive Turbulence Filter for Decomposition of Organized Turbulent Flows,” *Physics of Fluids*, Vol. 6, No. 5, 1994, pp. 1775–1786.

[34] Lumely, J., “Computational Modeling of Turbulent Flows,” *Advances in Applied Mechanics*, Vol. 18, 1978, pp. 124–176, 1978.

[35] Kourta, A., and HaMinh, H., “Turbulence et Aeroacoustique dans les Moteurs de Fusee,” *Conference on Propulsive Flows in Space Transportation Systems* (Bordeaux, France), 1995, pp. 464–477.

[36] Jones, W., and Launder, B., “The Prediction of Laminarization with a Two-Equation Model of Turbulence,” *International Journal of Heat and Mass Transfer*, Vol. 15, 1972, pp. 301–314.

[37] Chaouat, B., “Modelisation et Simulation des Ecoulements Turbulents dans les Propulseurs á Propergol Solide,” Thése de Doctorat de l’Universite Paris 6, Paris, France, 1994.

[38] Vuillot, F., Lupoglazoff, N., and Dupays, J., “Simulation Numerique du Detachement Tourbillonnaire dans un MPS: Premiére Validation sur le Cas C1xb 3mm brûles,” ONERA, TR RT 82/6133 EY, May 1996.